

Complexity of the Mw 6.3 2009 L'Aquila (central Italy) earthquake:

2. Broadband strong motion modeling

G. Ameri,¹ F. Gallovič,² and F. Pacor¹

Received 28 July 2011; revised 16 February 2012; accepted 26 February 2012; published 21 April 2012.

[1] Near-fault strong-ground motions (0.1–10 Hz) recorded during the Mw 6.3 2009 L'Aquila earthquake exhibit great spatial variability. Modeling the observed seismograms allows linking distinct features of the observed wavefield to particular source and propagation effects and provides insights on strong motion complexity from this moderate magnitude event. We utilize a hybrid integral-composite approach based on a k-square kinematic rupture model, combining low-frequency coherent and high-frequency incoherent source radiation and providing omega-squared source spectral decay. Several source model features, proven to be stable by means of an uncertainty analysis in the preceding low-frequency (<0.2 Hz) multiple finite-extent source inversion (Paper 1), were constrained. Synthetic Green's functions are calculated in a 1D-layered crustal model including 1D soil profiles to account for site-specific response (where available). The results show that although the local site effects improve the modeling, the spatial broadband ground-motion variability is to large extent controlled by the rupture kinematics. The modeling thus confirms and further constraints the source model features, including the position and slip amount of the two main asperities, the largest asperity time delay and the rupture velocity distribution on the fault. Furthermore, we demonstrate that the crossover frequency dividing the coherent and incoherent wavefield, often considered independent on the station position, has to be variable in order to adequately reproduce both near and far station recordings. This suggests that the incoherency of the radiated wavefield is controlled by the wave-propagation phenomena and/or the initial updip rupture propagation was very smooth (coherent) up to relatively high frequencies (>2 Hz).

Citation: Ameri, G., F. Gallovič, and F. Pacor (2012), Complexity of the Mw 6.3 2009 L'Aquila (central Italy) earthquake: 2. Broadband strong motion modeling, *J. Geophys. Res.*, 117, B04308, doi:10.1029/2011JB008729.

1. Introduction

[2] On April 6, 2009, at 1:32:40 UTC, a Mw 6.3 earthquake struck the L'Aquila city, one of the largest urban centers in the Abruzzo region (Central Italy), causing 308 casualties and large damage in the town and surrounding villages. The earthquake occurred along a NW-SE trending normal fault, 15–20 km long, dipping about 45° SW [Chiarabba *et al.*, 2009]. The hypocenter depth was estimated at about 9 km, located few kilometers southwest of the town center. This event represents the third largest earthquake recorded by strong motion instruments in Italy, after the 1980, Mw 6.9, Irpinia and the 1976, Mw 6.4, Friuli earthquakes.

[3] The earthquake has been recorded by several digital stations of the Italian Strong motion Network (*Rete*

Accelerometrica Nazionale, RAN), operated by the Italian Department of Civil Protection (DPC). The collected records represent a unique data set in Italy in terms of number and quality of records, azimuthal coverage and presence of near-fault recordings [Ameri *et al.*, 2009a; Zambonelli *et al.*, 2011].

[4] About 14 strong motion stations were located within 50 km from the earthquake epicenter, 5 of them within the surface projection of the estimated rupture plane. Detailed geological and geophysical information are available for these stations and are collected into the station monographs accessible through the Italian strong motion database (ITACA, <http://itaca.mi.ingv.it>). In particular, the site response characterization of stations in the epicentral area largely benefited from several research activities carried out after the earthquake, described by Gruppo di Lavoro M.S.-A.Q. [2010] and Cultrera *et al.* [2011]. An overview on site responses of the accelerometric sites, based on the analysis of strong motion recordings, is found in the work of Bindi *et al.* [2009].

[5] Despite the moderate magnitude of the L'Aquila earthquake, the strong motion data in the vicinity of the fault depict a large variability of the observed shaking. Previous

¹Istituto Nazionale di Geofisica e Vulcanologia, Milan, Italy.

²Faculty of Mathematics and Physics, Department of Geophysics, Charles University, Prague, Czech Republic.

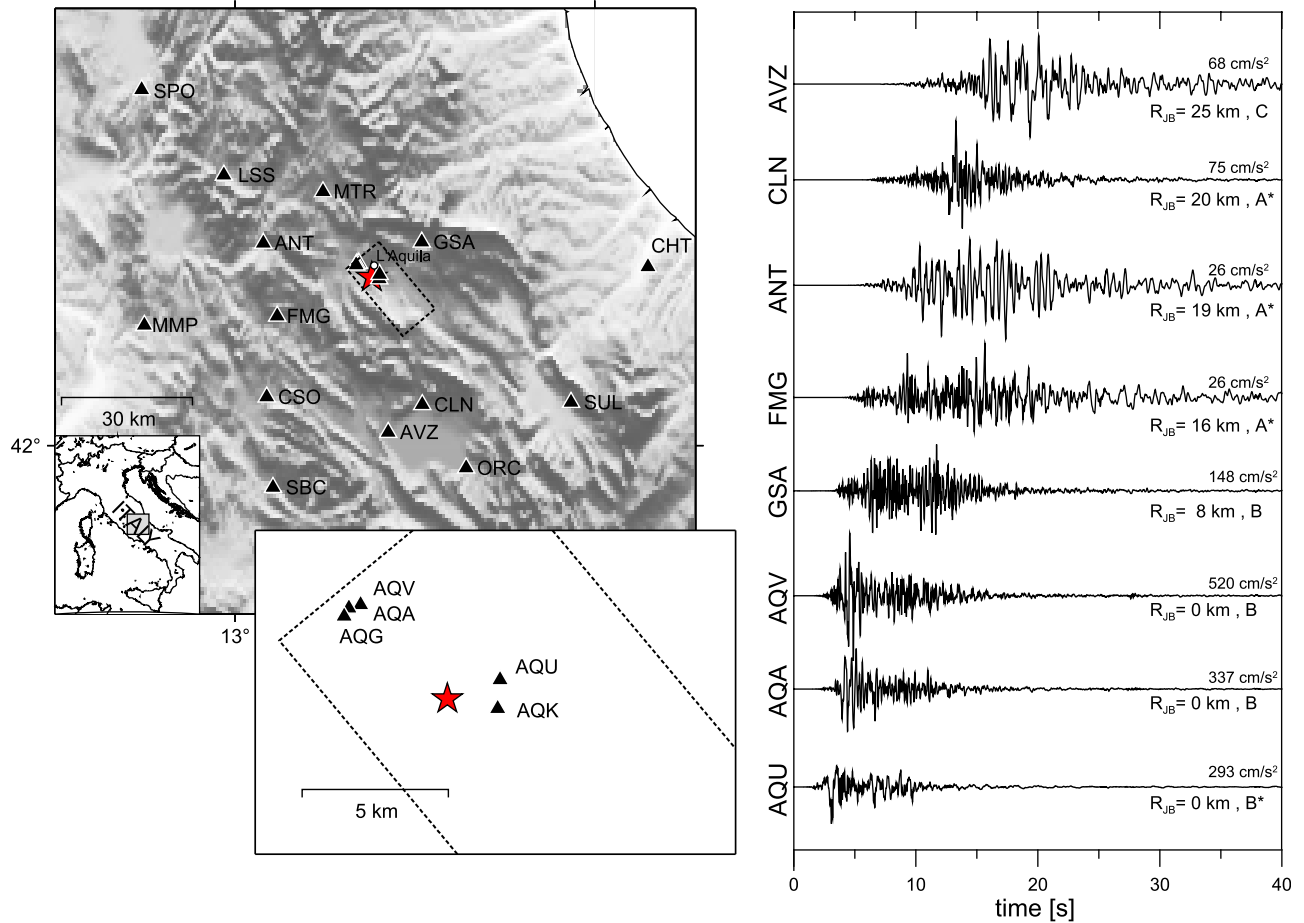


Figure 1. (left) Map showing the epicentral area of the 6 April 2009 L'Aquila earthquake. The strong motion stations are marked by triangles (see also Table 1). The inset shows a zoom on the near-fault (AQ_) stations. The earthquake epicenter and the surface projection of the rupture plane are indicated by the red star and the dashed rectangle, respectively. (right) Acceleration waveforms (North-South component), aligned on the earthquake origin time, recorded at selected sites around the fault. The peak ground acceleration values, the Joyner-Boore distance (R_{JB}) and the site classification according to EC8 are reported. Waveforms are band-pass filtered between 0.1 and 10 Hz.

studies have shown that, although local site effects and wave propagation influenced the ground motion characteristics, the rupture process substantially contributes to the spatial distribution of the observed ground motion [Ameri *et al.*, 2009a; Akinci *et al.*, 2010]. Source inversion studies performed for the L'Aquila earthquake using strong motion and geodetic data showed that the rupture followed a complex pattern with a slip distribution composed by at least two asperities and a variable rupture velocity over the fault plane [Cirella *et al.*, 2009; D'Amico *et al.*, 2010; Scognamiglio *et al.*, 2010]. Newly introduced multiple finite-extent inversion applied to the L'Aquila data, see the companion paper [Gallovič and Zahradník, 2011] (hereinafter referred to as Paper 1), confirmed the two major slip patches and suggested temporal delay (~ 3 s) of the deeper one.

[6] Broadband ground motion simulation techniques based on kinematic rupture models can be used to study the effect of source complexity on strong ground-motion records. Most of such methods simulate the ground motion by combining the synthetics computed with deterministic and stochastic (or

semi-stochastic) approaches for the low- and high-frequency parts, respectively [e.g., Pitarka *et al.*, 2000; Mai and Beroza, 2003; Gallovič and Brokešová, 2007; Hisada, 2008; Ameri *et al.*, 2008; Mai *et al.*, 2010; Graves and Pitarka, 2010]. These techniques are used to investigate past earthquakes [e.g., Aagaard *et al.*, 2008; Ameri *et al.*, 2009b] as well as to perform scenario-events studies [e.g., Graves *et al.*, 2011].

[7] One of the advantages of using forward modeling is that the effect of source input parameters on observed motions can be controlled and assessed individually. In this way, the most critical input parameter (if any) controlling the fit with the observed ground motion at a given station can be identified and insights on the source process can be retrieved by minimizing the difference between observed and simulated ground motions.

[8] In this study we investigate the ground-motion complexity observed during the 2009 L'Aquila earthquake performing broadband ground-motion simulations with a hybrid integral-composite technique based on a k^{-2} rupture model [Gallovič and Brokešová, 2007]. Starting from the

Table 1. Strong Motion Stations Considered in This Study

Code	Station Name	Longitude (°E)	Latitude (°N)	R _{epi} (km)	R _{JB} (km)	Site Class EC8 ^b
AQG ^a	L'Aquila-Colle Grilli	13.3370	42.3735	4.10	0.00	B
AQA ^a	L'Aquila-F. Aterno	13.3390	42.3760	4.20	0.00	B
AQV ^a	L'Aquila-Centro Valle	13.3439	42.3771	3.99	0.00	B
AQK	L'Aquila-Aquil Park	13.4010	42.3450	2.13	0.00	B
AQU	L'Aquila-Castello	13.4019	42.3539	2.18	0.00	B*
GSA ^a	Gran Sasso (Assergi)	13.5194	42.4207	14.15	8.59	B
MTR	Montereale	13.2448	42.5240	22.13	15.93	A*
FMG	Fiamignano	13.1172	42.2680	23.17	16.56	A*
ANT	Antrodoco	13.0787	42.4182	25.54	19.31	A*
CLN	Celano	13.5207	42.0852	31.79	19.95	A*
AVZ ^a	Avezzano	13.4259	42.0275	36.15	25.14	C
CSO	Carsoli	13.0881	42.1009	36.45	31.68	A*
LSS	Leonessa	12.9689	42.5583	40.62	35.63	A*
ORC	Ortucchio	13.6424	41.9536	49.19	37.34	A*
SUL	Sulmona	13.9343	42.0895	54.29	43.35	C*
MMP	Mompeo	12.7483	42.2492	52.86	45.87	A*
SBC	Subiaco	13.1055	41.9132	53.45	46.59	A*
CHT	Chieti	14.1478	42.3698	63.47	52.17	B
SPO	Spoletto	12.7406	42.7336	67.30	62.60	A*

^aStation for which 1D site-specific soil profiles are used. See main text and Figure 3.

^bEC8 classes with asterisks are attributed on the basis of geological/geophysical information (<http://itaca.mi.ingv.it/ItacaNet/>).

basic features of the multiple finite-extent inversion results, based on strong motion data at frequency below 0.2 Hz (see Paper 1), we “extend” the source model to higher frequencies, calculate broadband (0.1–10 Hz) synthetic seismograms and compare them with the recorded ground motions. We show that most of the observed complexity can be explained when properly combining site-specific and finite-fault effects. In particular, we test the effects of the rupture delay of the largest asperity, rupture velocity values, small-scale slip distribution and local site response. Finally, we investigate the relative contribution of coherent (i.e., deterministic) and stochastic processes in the ground-motion generation at different sites.

2. The April 6, 2009 L'Aquila Earthquake: Strong Motion Records

[9] The L'Aquila earthquake provided the most extensive set of high-quality near-fault strong motion records ever recorded in Italy for such a major event. It has been recorded by 14 stations within 50 km from the epicenter, 5 of them within the surface projection of the estimated rupture plane at distances less than 5 km from the epicenter (Figure 1 and Table 1). Three of these stations are part of an array deployed in the upper Aterno-river valley (AQG, AQA and AQV) whereas the other two (i.e., AQK and AQU) are in downtown L'Aquila. In the following we will refer to this group of near-fault stations simply as “AQ_.”

[10] In Table 1, the sites are classified according to the Euro-code 8 [Comité Européen de Normalisation, 2004] and the Italian Building Code (http://www.cslp.it/cslp/index.php?option=com_docman&task=doc_download&gid=3255&Itemid=10) based on the shear wave velocity averaged over the top 30 m of the soil profile - $V_{s,30}$. The EC8 class each station has been attributed on the basis of direct measure of $V_{s,30}$ or on geological/geophysical information [Di Capua, 2009; Di Capua et al., 2011].

[11] The acceleration waveforms at eight stations distributed around the fault are shown in Figure 1 (right), pointing out the remarkable azimuthal dependence of recorded ground

motions in terms of peak values, frequency content, envelope, and durations. The closest stations, AQU, AQV and AQA, few kilometers apart, have similar durations although the peak values and frequency content vary. GSA and FMG accelerations, recorded at similar epicentral distance on the footwall and hanging wall sides of the fault, respectively, display remarkable differences in peak values (more than 5 times larger at GSA than at FMG), duration and frequency content. Moreover, at both stations, but to a larger extent at GSA, the waveforms show two distinct wave packets of similar amplitudes that are not equally well visible on the other records. Stations ANT, CLN and AVZ are approximately located at similar distances, in the strike direction (NW-SE), but on opposite sides of the fault. Again, the records show substantial differences. The peak acceleration reported at ANT is 3 times smaller than that at the other two stations while CLN record has smaller duration.

[12] The complexity observed in the accelerations time series, can be also found in the velocity waveforms. The AQ_ records are all characterized by pulses at the beginning of the signal that have been interpreted as near-source effects [Ameri et al., 2009a; Chioccarelli and Iervolino, 2010].

3. Methodology

[13] For the strong ground-motion modeling we use hybrid integral-composite (HIC) approach introduced by Gallovič and Brokešová [2007]. This model is designed mostly for the earthquake ground-motion simulations, providing omega-squared source spectrum. It is based on techniques developed by Andrews [1980], Herrero and Bernard [1994], Zeng et al. [1994], Gallovič and Brokešová [2004], among others.

[14] The source model is divided into subsources with number-size distribution characterized by fractal dimension $D = 2$. For simplicity, the subsources are assumed rectangular with sizes given by integer fractions of the fault length L and width W , i.e., of sizes $L/n \times W/n$, where level $n = 2 \dots N$ (in the present calculations we assume $N = 8$). Assuming constant stress drop scaling, the slip of the subsources is

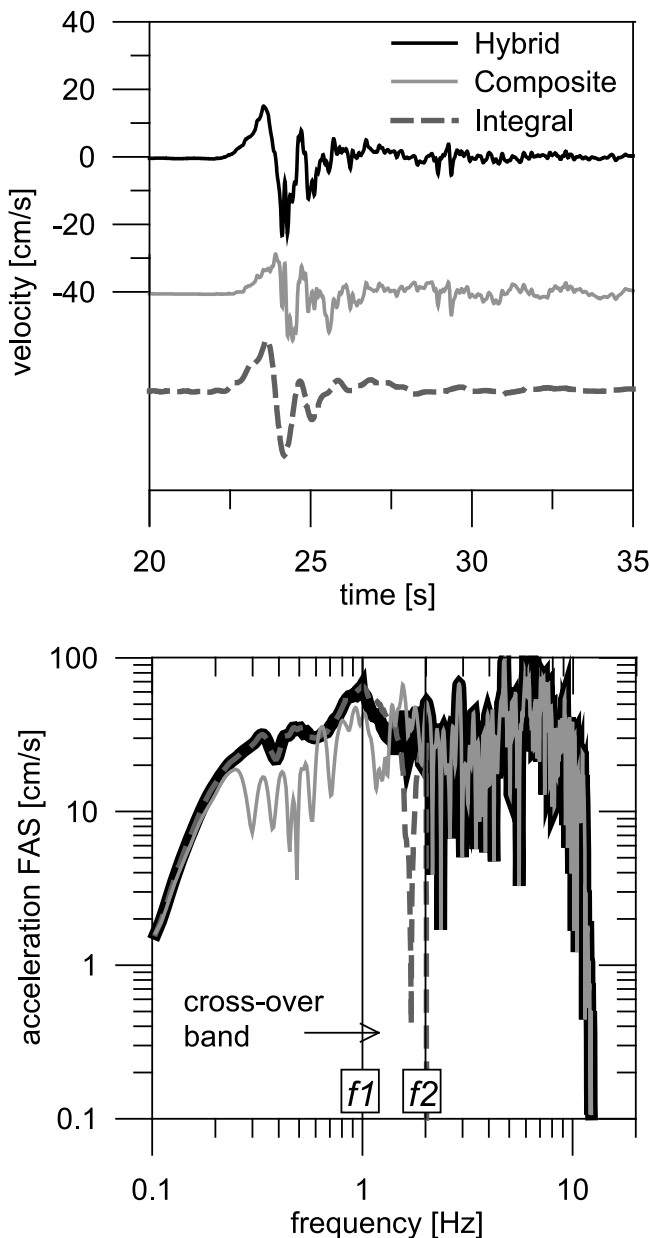


Figure 2. Example of calculation of hybrid broadband seismograms by combining integral and composite approaches. (top) Velocity seismograms and (bottom) Fourier amplitude spectra (FAS) from hybrid, composite and integral approaches. The combination of integral and composite seismograms is performed in the crossover frequency band (between bounding frequencies f_1 and f_2), where the synthetics spectra (both real and imaginary parts) are multiplied by weighting functions $\sin^2(x)$ and $\cos^2(x)$, with $x = (\pi/2)((f - f_1)/(f_2 - f_1))$ and summed up (see Gallovič and Brokešová, 2007). The figure shows that the hybrid seismogram contain more complexity than the integral one, while enhancing (coherent) directivity effect with respect to the composite one.

reciprocally proportional to the level n . For the particular number-size distribution the number of subsources at level n equals to $2n-1$. For $n > 2$ the subsources are distributed randomly over fault plane with possible overlap.

[15] Assuming that the subsources are characterized by statistically the same slip distribution (i.e., they are self-similar), the resulting slip distribution over the whole fault has k -squared decay at high wave numbers k [Andrews, 1980]. Thus, we prescribe k -squared slip distribution on each of the subsources to mimic that it is again composed of smaller subsources. To simulate the source radiation being coherent at small wave numbers and incoherent at large ones, we divide the calculations into two frequency bands. In the low-frequency band we use the representation theorem (integral approach). This utilizes the k -squared slip distribution composed by the subsources and delta function as the slip velocity function. In the high-frequency range, we assume that the subsources radiate Brune's source time functions with proper seismic moment and corner frequency given by the sizes of the subsources, measured from their centers (composite approach). Note that the same set of subsources is used in both the integral and composite parts of the simulations. This way, the directivity effect is modeled in the low frequency range, while it disappears at high frequencies due to the incoherent summation of the contributions of subsources [Gallovič and Burjánek, 2007]. Such model is thus in agreement with the engineering expectation of directivity derived from the regressions of recorded ground motions of moderate-to-large earthquakes [Somerville et al., 1997; Spudich and Chiou, 2008] showing that directivity-induced amplification of ground motion can be recognized only in the low-frequency range (roughly below 1–1.5 Hz). However, whether these effects actually vanish at high frequencies due to rupture incoherencies and above which frequency they are no longer significant it is still a matter of debate [Boatwright, 2007; Cultrera et al., 2009]. In order to also reduce the effect of the radiation pattern at high-frequencies we assume $\pm 30^\circ$ random variations of the strike, dip and rake angles of the subsources in the composite part of the calculations.

[16] The integral and composite calculations are crossover combined in a given frequency band (see illustration in Figure 2). Note that this band implies up to which frequency the directivity effect is modeled. In the present paper we test several choices of the crossover band.

[17] The Green's functions for both calculations are computed by the discrete wave number technique, DWN [Bouchon, 1981], either in general 1D layered model or in specific 1D models for the individual stations that include low-velocity subsurface layers, where available. The DWN technique provides full wavefield Green's functions; no stochastic Green's functions are used.

4. Crustal Propagation Model and Site Effects

[18] In order to calculate the Green's functions in the study region we use the 1D velocity model proposed by Bianchi et al. [2010], based on receiver function analyses. We adopt the model derived at the FAGN station (belonging to the National Seismic Network (RSN, INGV-CNT) and localized close to the southeastern termination of the fault) because it is found in preliminary analysis to be more appropriate to

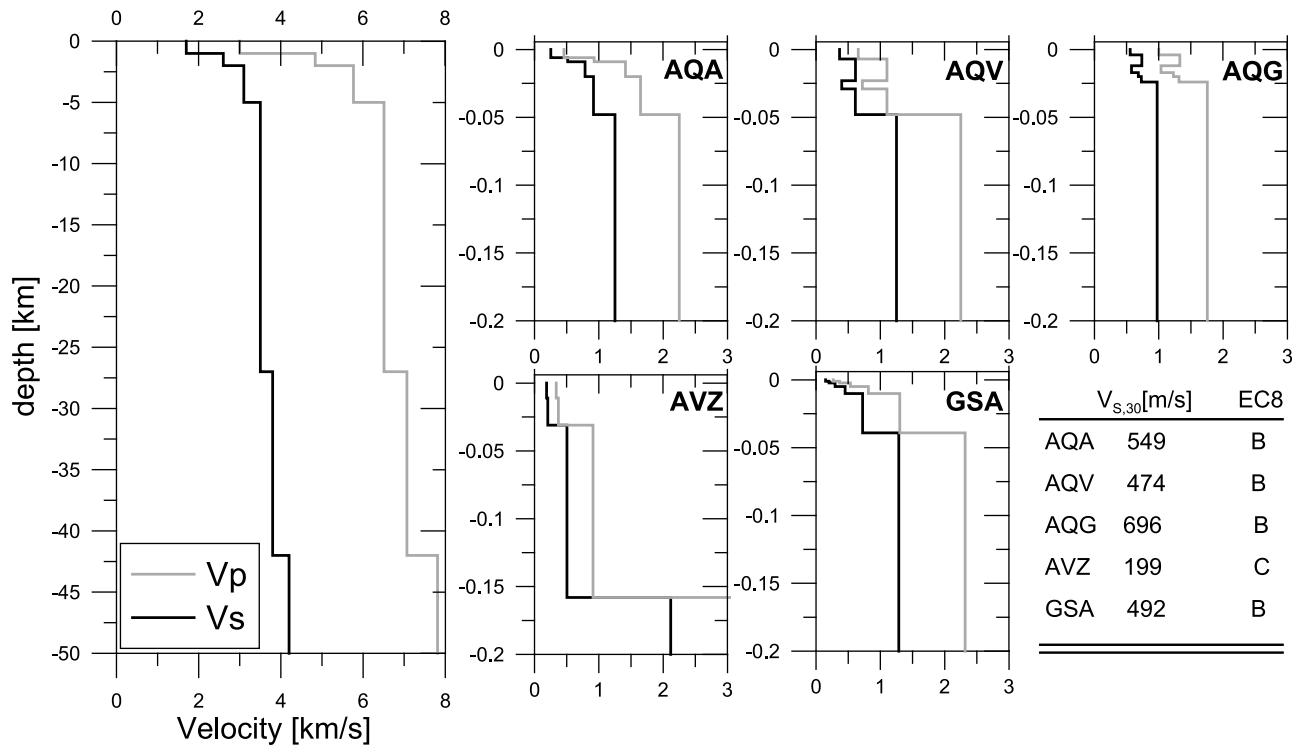


Figure 3. The 1D velocity models used in the simulations. (left) Velocity profile used for the L'Aquila region (see Table 2). (right) Site-specific shallow soil profiles adopted at the respective stations (the profiles extend downward according to the regional model shown in Figure 3, left). The velocities have been measured through downhole and cross-hole tests at AQA, Aqv and Aqg and estimated with Multichannel Analysis of Surface Wave (MASW) at GSA and AVZ (<http://itaca.mi.ingv.it/ItacaNet/>). The $V_{s,30}$ values and the EC8 site classes for these stations are also indicated.

represent the general wave propagation over the whole study area (Figure 3, left and Table 2). The authors also provide another V_s profile for AQU station. The two models reveal strong differences for the shallow crust, whereas deeper features are similar. As reported by *Bianchi et al.* [2010], the very high V_s values (>4 km/s) found underneath AQU are a localized feature absent beneath the FAGN station where V_s values are within limits usually observed for carbonate rocks.

[19] Beside the regional wave propagation characteristics we need to account, in the simulated seismograms, for the effect of amplification (or de-amplification) of seismic waves occurring in the shallow-most soil layers (i.e., in the last tens of meters). Such effects are known to significantly modify the amplitude, frequency content and duration of the ground motion at the surface and should to be considered to model the observed ground motion.

[20] Despite all the available information, to decide how to include site effects in the modeling is not straightforward. The appropriate way would be to calculate the Green's functions for site-specific soil profile at each station. However, this approach conflicts with the fact that soil profiles are not available at most of the stations. Other commonly used approaches that do not require the knowledge of the soil profile utilize empirically derived amplification functions either based on reference site methods or on single-stations measurements. However, such functions generally describe the amplification of Fourier amplitude spectra only and do not provide information of phase modifications. Moreover,

the reliability of the amplification curves depends on the number and quality of available records at the stations or on the adopted reference rock site.

[21] In this paper, we opt for incorporation of site response only by including site-specific 1D soil layers in the crustal model; for five of the closest stations to the epicenter (Figures 1 and 3, Table 1) such 1D profiles are available (<http://itaca.mi.ingv.it/ItacaNet/>). In particular, stations AQA and Aqv are installed on the recent alluvial deposits of the Aterno river, made of gravels alternated to thin layers of finer deposits, that reach the seismic bedrock, defined by shear velocities larger 800 m/s, at depth of about 30 m and 50 m, respectively (see *Puglia et al.* [2011] and *Lanzo et al.* [2011] for details). Station Aqg is installed on limestones

Table 2. Velocity Model Used for the L'Aquila Region^a

Depth (km)	V_P (km/s) ^b	V_S (km/s)	ρ (g/cm ³)	Q_P	Q_S
0	3.16	1.70	2.50	200	100
1	4.83	2.60	2.84	400	200
2	5.76	3.10	2.94	400	200
5	6.51	3.50	3.15	400	200
27	7.00	3.80	3.26	600	300
42	7.80	4.20	3.50	800	400

^aThe model is based on the *Bianchi et al.* [2010] V_s profile for station FAGN. We simplified their V_s profile by removing the velocity inversion in the deep layer (between 13 and 19 km).

^bValues are computed as $V_P = V_S \cdot 1.86$.

Table 3. Parameters Used in the Modeling

Parameter	Value	Input Parameter ^a
Fault mechanism	strike: 140°, dip: 50°, rake: −90°	IC
Fault dimensions	length 20 km, width 15 km	IC
Fault top depth	0.5 km	IC
Focal depth	9.0 km	IC
Seismic moment	2.5×10^{18} N m	IC
Stress drop	100 bars	C
Nucleation point (position from northwestern edge)	downdip: 11 km, along strike: 6 km	IC
Rupture velocity (Vr)	2 km/s (above 5 km depth) 3 km/s (below 5 km depth)	IC
Risetime	0.1 s	I
Number of subsource levels	8	IC
Total number of subsources	63	IC
Crossover frequency band	1.5–2.0 Hz (AQ ₊ stations) 0.3–0.6 Hz (other stations)	IC
Discretization of the fault plane	130 × 100 point sources	I

^aI, C, and IC show whether the input parameter affects the Integral, Composite or both parts of the calculated waveform.

and marly limestones and the seismic bedrock is reached at depth of 20–30 m. The GSA station is located on stiff soils (limestone and marls), the velocity profile shows some velocity increase in the first 10 m and a deeper layer with Vs of about 600 m/s down to 40 m. Below, a faster layer with a shear velocity of 1300 m/s is reported. Station AVZ is located on alluvial deposits and the Vs profile is characterized by a low velocity layer (about 200 m/s) for the first 35 m and a deeper layer with Vs of about 500 m/s that extends down to 160 m where the bedrock is found. For the remaining stations, the synthetics are computed using the 1D crustal model reported in Table 2 having a shear velocity at surface equal to 1700 m/s, without including site-specific effects.

[22] To properly describe the high-frequency spectral decay of synthetics, we adopt the κ operator, introduced by *Anderson and Hough* [1984]. We set $\kappa = 0.03$ s, that is a typical value for rock sites in central Italy [*Bindi et al.*, 2004].

5. Hybrid Source Model

[23] The source characteristics of the L'Aquila earthquake have been deeply investigated and a number of source models have been proposed based on analyses of strong motion, teleseismic, GPS, SAR and field data [*Anzidei et al.*, 2009; *Atzori et al.*, 2009; *Cirella et al.*, 2009; *Falcucci et al.*, 2009; *D'Amico et al.*, 2010; *Scognamiglio et al.*, 2010]. The rupture dimensions and location of the main slip patch are approximately shared by the various models.

[24] In this paper we use the same fault plane and mechanism as in Paper 1, i.e., a rectangular fault plane 20 km long and 15 km wide having a strike of 140° and dipping 50° toward southwest. The rake angle is −90° (pure normal-fault mechanism) and the hypocentral depth is 9 km (Table 3). Such fault geometry and focal mechanism essentially agree with all the previous studies. We constrain the basic features of the kinematic rupture model according to the low-frequency inversion performed in Paper 1: namely (1) the approximate location of the two main asperities, (2) the time delay of the southeastern asperity rupture, and (3) the decrease of rupture velocity in the shallow parts of the fault.

[25] The final HIC source model used to calculate synthetic seismograms up to 10 Hz is reported in Figure 4. The rupture time distribution is obtained assuming two rupture velocities (as marked also in Figure 4) and a nucleation point corresponding to the instrumental hypocenter. As suggested by the slip inversion, a rupture delay of the southern asperity by approximately 3 s is also included in the model. Although the low-frequency inversion suggests that the shallower subsource ruptured with a lower velocity than the deeper ones, the results show poor sensitivity to rupture velocity values. For this reason we test different values and set the final rupture velocity in the bottom and top part of the fault equal to $V_r = 3$ km/s and $V_r = 2$ km/s, respectively. Note that these values roughly corresponds to 85% of the average shear wave velocity at the relative depths.

[26] The final slip distribution is obtained constraining the positions of the three largest subsources (at level $n = 2$), that are characterized by the largest seismic moment, according

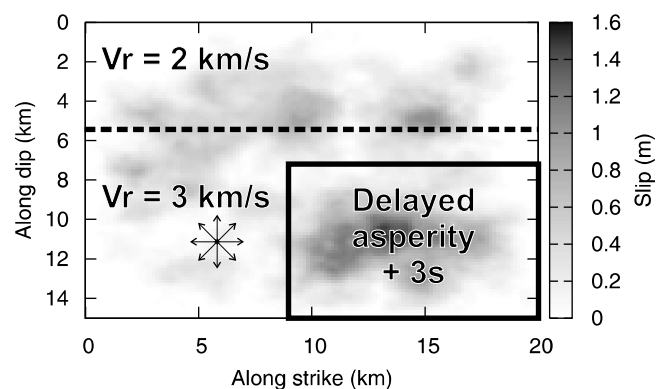


Figure 4. Kinematic rupture model used in the simulations. The final k-squared slip distribution composed of slip contributions from the fractal subsources is mapped by gray tones. The rupture velocity (V_r) values used in the top and bottom part of the fault as well as the location of the delayed asperity are illustrated. The outward vectors indicate the rupture nucleation point. The positions of the three largest subsources (at level $n = 2$) centers are: (8, 6), (12, 11) and (15, 11).

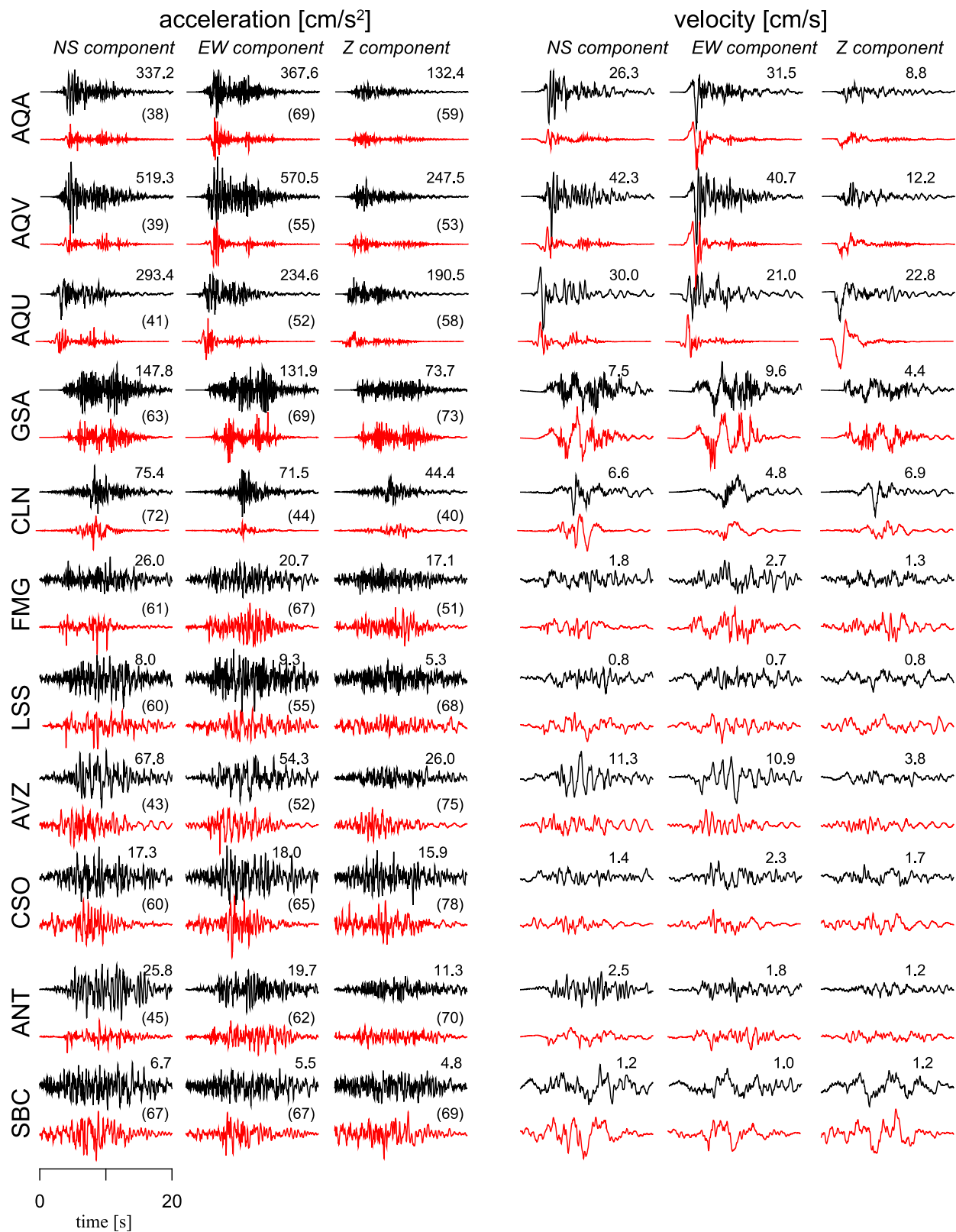


Figure 5. Comparison of recorded (black) and simulated (red) broadband three-component (left) ground-acceleration and (right) velocity waveforms at 11 selected sites (indicated in Figure 1) for the L'Aquila earthquake. North-South, East-West and vertical components are shown. The recorded and simulated motions for each station are scaled to the maximum value listed above each pair of waveforms. The numbers between brackets are the goodness-of-fit score. Waveforms are band-pass filtered between 0.1 and 10 Hz. Comparison for other stations is presented in the Supporting material.

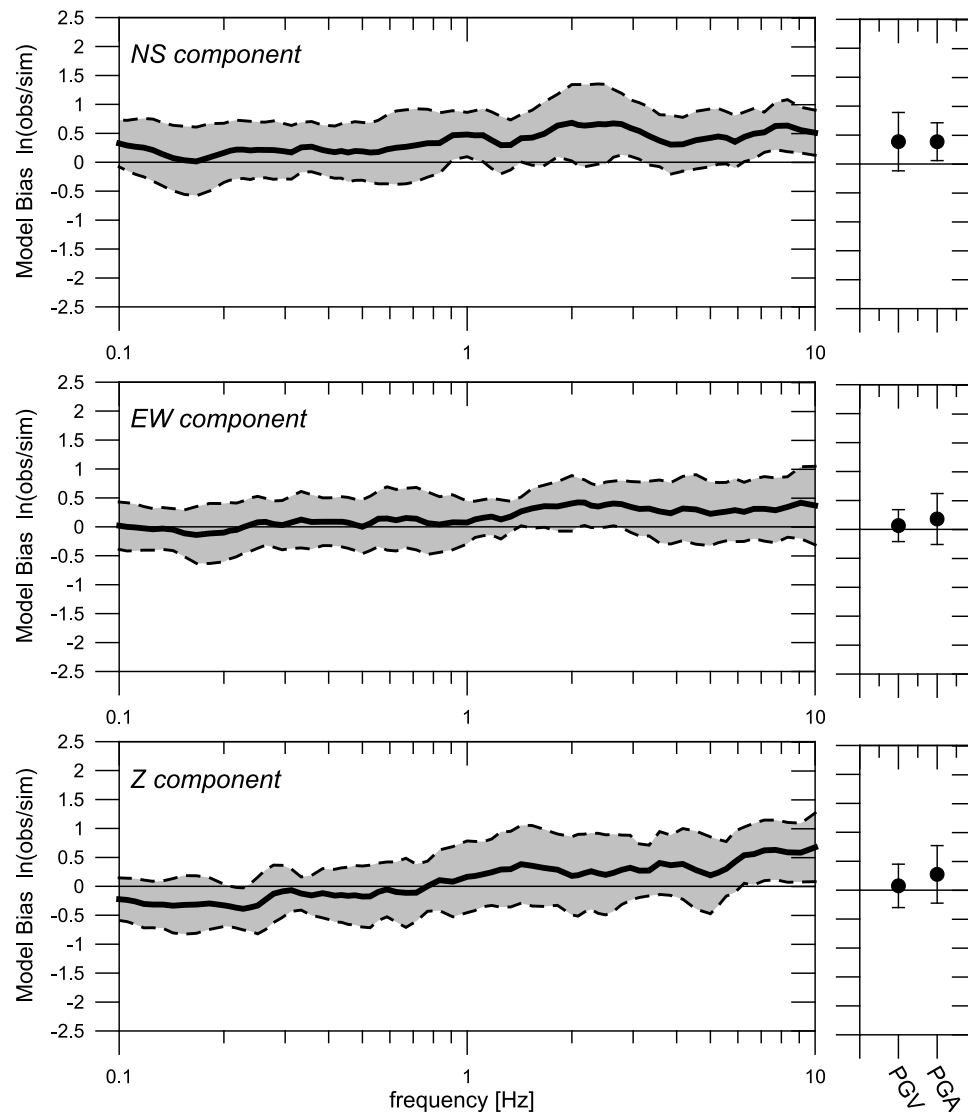


Figure 6. (left) Model bias (thick line) and standard deviation (shaded region) for 5% damped spectral acceleration using 15 sites for the L'Aquila earthquake. (right) Model bias and standard deviation for peak ground velocity (PGV) and peak ground acceleration (PGA) are also shown. (top) North-South component, (middle) East-West component, and (bottom) vertical component. Note that in the calculations we excluded 4 stations clearly problematic (i.e., MTR, SUL, ORC, CHT in the auxiliary material).

to Paper 1. In particular, one of them is placed “above” the hypocenter and the other two are set in the southern bottom part of the fault. At levels higher than 2, the remaining 60 subsources are randomly distributed over the fault plane following the defined number-size distribution, composing random high-wave numbers details of the slip distribution.

[27] Finally, the stress drop of the whole event is set to 100 bars based on estimates by *Bindi et al.* [2009] and on comparison between observed and synthetic high-frequency level of the Fourier amplitude spectra (see an example in the auxiliary material).¹

[28] Note that, since the main features of this model are retrieved by the low-frequency inversion, the success of the

broadband modeling depends on whether or not the observed high-frequency ground motions are affected/controlled by the low-frequency source features.

6. Results: Modeling of Strong Motion Records

[29] The HIC method allows for relatively fast ground-motion simulations, thus we performed a large number of trial calculations with the aim to obtain the “best fit” with recorded data. The sensitivity of the results to the local site response, rupture velocities, slip distribution at high wave numbers, rupture delay of second asperity and crossover frequency between the integral and composite approaches is investigated. Some of these results at specific sites will be discussed in the next paragraphs. Note that no artificial site-dependent time shifts were made because the recordings are accompanied by correct timings.

¹Auxiliary materials are available in the HTML. doi:10.1029/2011JB008729.

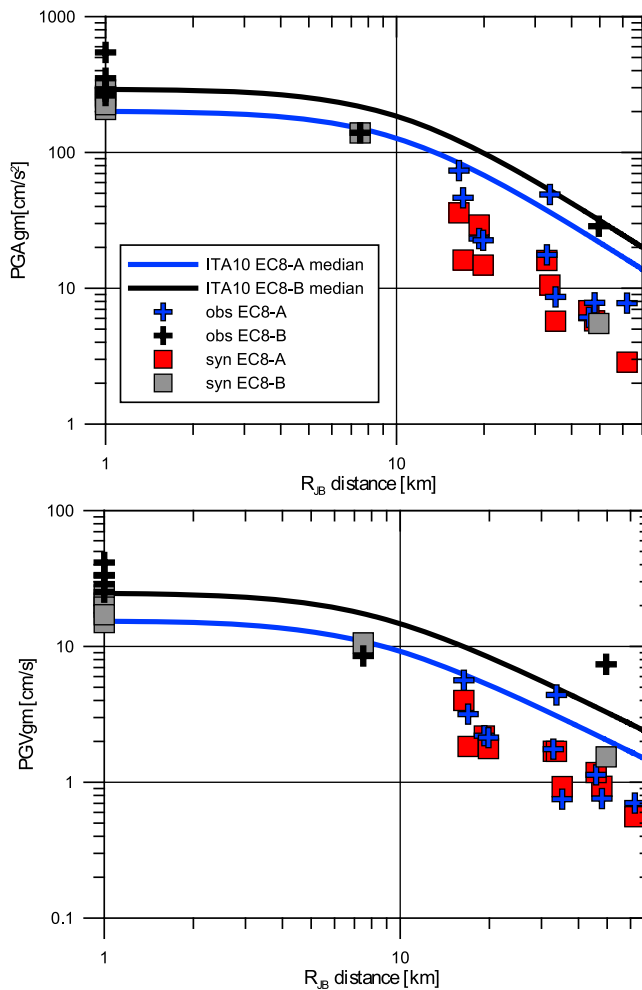


Figure 7. Observed (crosses) and simulated (squares) PGA and PGV (geometric mean of NS and EW components) as a function of Joyner-Boore distance (R_{JB} , minimum distance from the site and the surface projection of the rupture plane). Median estimates from *Bindi et al.* [2011] GMPEs (ITA10) are also shown. The symbols and lines colors represent the corresponding EC8 site class.

[30] The fit is judged according to the goodness-of-fit (GOF) criteria defined by *Olsen and Mayhew* [2010]. They proposed a GOF algorithm based on different metrics, among which we selected: Peak Ground Acceleration (PGA), velocity (PGV) and displacement (PGD), response spectral acceleration and smoothed Fourier spectrum averaged for periods between 0.1 and 10 s, energy duration 5–75% and cumulative kinetic energy. More details on the definition and selection of the different metrics can be found in the work of *Olsen and Mayhew* [2010]. The final GOF score is defined as GOF average (from 0 to 100) of the equally weighted abovementioned metrics.

[31] Based on these criteria, we define a so-called best model, whose main parameters are listed in Table 3. Figure 5 presents an overview of the modeling results for this model, showing comparison of synthetic and observed acceleration and velocity waveforms for 11 selected stations (Table 1 and Figure 1). The GOF score is reported for each station and each

component. Both the observed and simulated waveforms are band-pass filtered between 0.1 and 10 Hz. The results for all the stations are reported in the auxiliary material (Figures S1–S9), also including the comparison of observed and simulated Fourier amplitude spectra (FAS).

[32] In general, the synthetics reproduce well the observed waveforms, despite the simplicity of the propagation models and the lack of site response for the most of the stations. The duration of the strong motion phase is well reproduced as well as the acceleration and velocity peak values. Concerning near fault sites (AQ_ stations), the synthetics show the characteristic velocity pulses with amplitude similar to the observed ones, at least on one component. However, an underestimation in the amplitudes and a lack of some high-frequency phases is noticed on the horizontal components (particularly on the North-South one), suggesting that more complex effects related to the presence of Aterno valley or details of source rupture model could affect the ground motion at these sites.

[33] A comparison between observed and simulated acceleration response spectra (5% damping) and acceleration and velocity peak values, PGA and PGV, is presented in Figure 6. For the best model, residuals are calculated as $\ln(Y_{\text{obs}}/Y_{\text{sim}})$, where Y is the ground-motion parameter ($SA(f)$, PGA, or PGV). The residuals are computed considering 15 out of the 19 stations presented in Table 1, excluding four stations (CHT, MTR, ORC and SUL) that are characterized by dominant site-specific phenomena, not explainable with the considered propagation model (see figures in the auxiliary material). The model bias is obtained by calculating the mean and standard deviation of the residuals over all stations for the considered ground-motion parameters. Figure 6 presents the model bias separately for horizontal and vertical components. A model bias of zero indicates that the simulation, on average, matches the observed ground-motion level. A negative model bias indicates overprediction of the observations and a positive model bias indicates underprediction of the observations.

[34] The comparisons shown in Figure 6 exhibit little systematic model bias across a wide frequency range. The standard deviation ranges from about 0.3 to 0.7 natural log units. There is a tendency to underestimate spectral ordinates above 1 Hz on all components that can be ascribed to the lack of site-specific amplifications at most of the stations. Only for the NS component the underestimation extends also to lower frequencies. As mentioned above, such underestimation is related to the AQ_ stations.

[35] Figure 7 compares the observed and simulated PGA and PGV (geometric mean of NS and EW components) as a function of distance. The distance-decay of the observed peak values is well described by the synthetic ones, although at few stations, where the site-specific effect is not considered, the underestimation is remarkable (examples are ORC and CHT stations, see the waveform comparisons in the auxiliary material). The peaks are also compared with estimates from empirical ground motion prediction equations (GMPEs) for the Italian territory [*Bindi et al.*, 2011]. Interestingly, the decay of the observed amplitudes for rock sites (EC8 class A) is better described by the simulated values than by the median estimates from the adopted GMPEs, at least over the distance range considered in our modeling. This result indicates that the ground motion in the epicentral

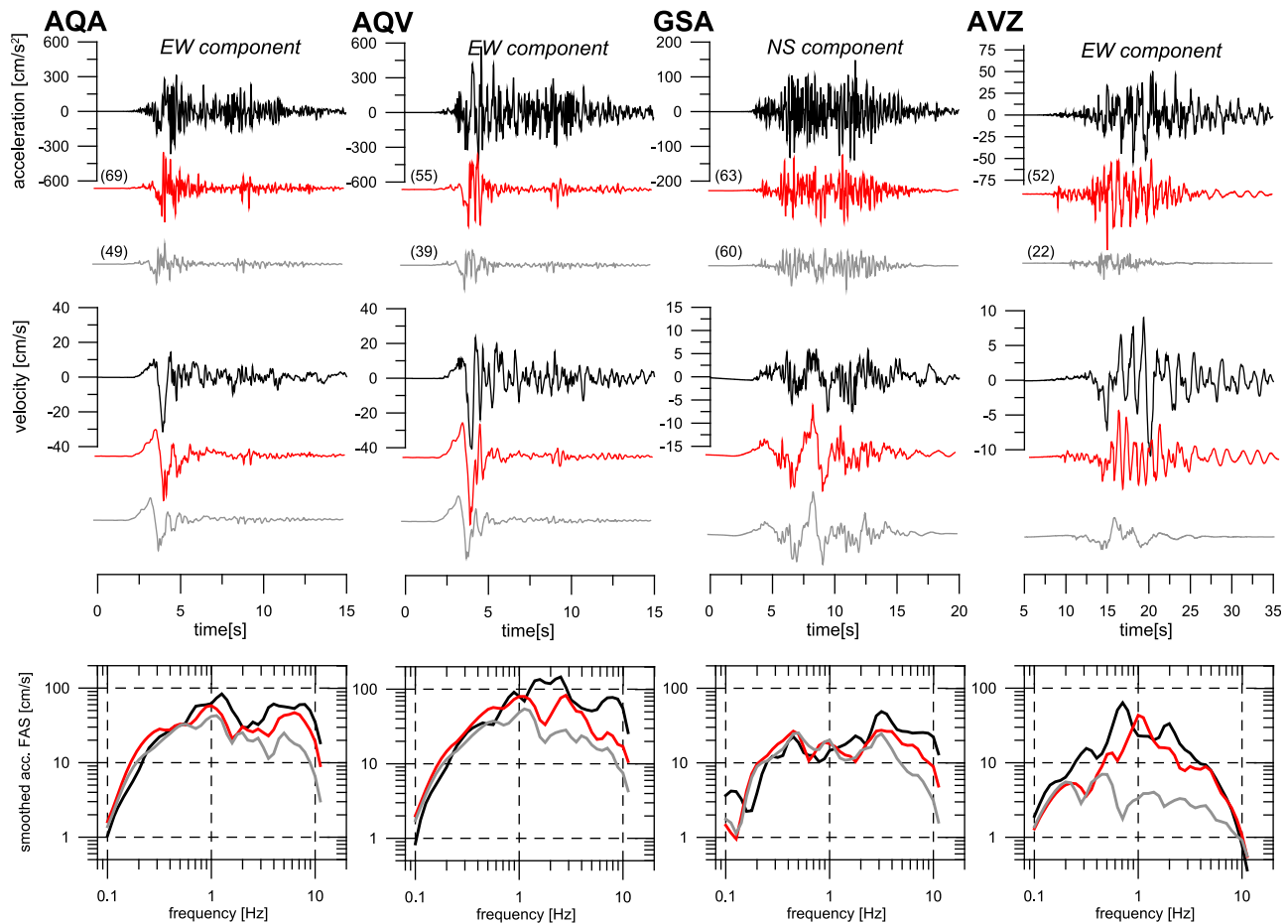


Figure 8. Effect of the subsurface site-specific soil profiles. (top, middle) Recorded (black), best model (red) and no-site-effects model (gray) ground-acceleration and velocity waveforms (one horizontal component) at four selected sites (indicated in Figure 1). The numbers between brackets are the goodness-of-fit score. (bottom) Corresponding smoothed acceleration Fourier amplitude spectra (FAS).

area of the L'Aquila earthquake attenuates faster than what prescribed by the GMPEs for similar magnitude earthquakes.

[36] In the following we discuss some interesting features of the modeling, illustrating the distinct sensitivity of individual station recordings to various properties of the source/propagation models. We mostly concentrate on near-fault stations, especially those with available 1D soil profile.

6.1. Effect of 1D Soil Profiles

[37] As explained in section 4, at five stations we simulate the ground motion including a 1D site-specific subsurface structure (see Figure 3). The introduction of the site-specific soil profile into calculation of the Green's function allows to better evaluate the site effects, taking implicitly into account the incoming wavefields with proper incident angles at the base of the profile.

[38] Figure 8 illustrates the importance of including such site-specific shallow layers to reproduce spectral amplitudes and waveform durations. Synthetic acceleration and velocity seismograms and acceleration FAS, calculated including or not the 1D soil profiles (red and gray color in Figure 8, respectively), are compared with observed ones at four sites. Indeed, the soil response effectively enhances the ground

motions, especially above 1 Hz (see the comparisons of FAS in Figure 8, bottom).

[39] The most dramatic effect is observed at station AVZ where the FAS are increased 5–10 times over a broad frequency band. Accordingly, the velocity and acceleration wavefields are also enhanced, however, by a smaller factor. The large amplifications of the FAS is also due to the modeling of later phases generated by the wave propagation in the shallow layers, resulting in longer duration of the simulated records. The large amplification and duration lengthening at AVZ station are caused by the thick soft sediments of the Avezzano Plain over which the station is located. Site amplification effects at AVZ are also clearly recognized by empirical studies [Bindi *et al.*, 2009] that reported large amplifications (>5) for frequencies around 1 Hz.

[40] At the other stations the effect of the adopted 1D soil profile is lower. The durations are more or less preserved. The shape of velocity synthetics is only slightly modified (see, e.g., station GSA). In particular, at AQA and AQV, the large-amplitude waves between the wave packages coming from the two asperities remain unexplained. These differences are related to features not included in the adopted model, such

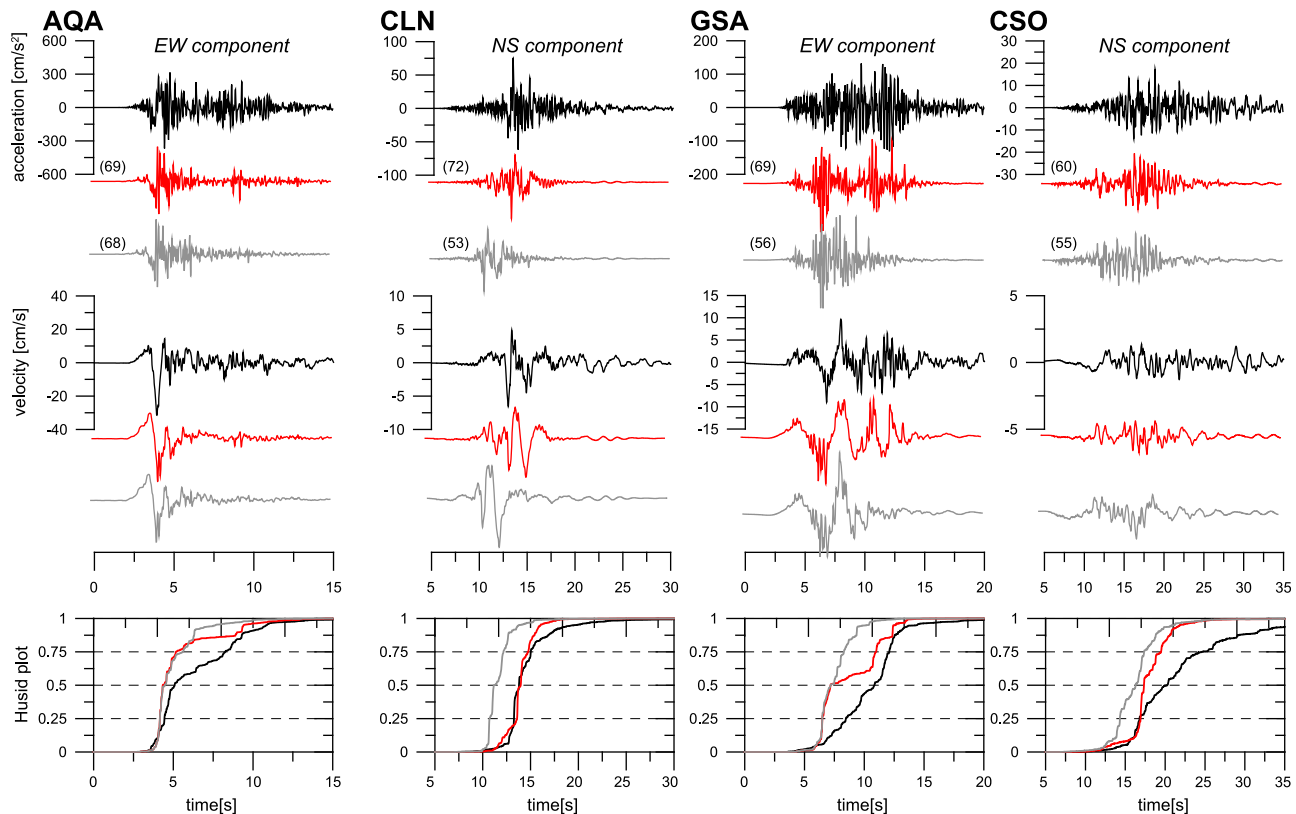


Figure 9. Effect of the asperity delay. (top, middle) Recorded (black), best model (red) and no-asperity-delay model (gray) ground-acceleration and velocity waveforms (one horizontal component) are compared at four selected sites (for their position see Figure 1). The numbers between brackets are the goodness-of-fit score. (bottom) Respective normalized Husid plots (cumulative squared acceleration).

as 3D crustal effects and/or additional complexities of the source model. The latter might be related to rupture propagation effects that we substitute in our model by the delay of the second asperity (see next section). Equally, there might be some slip complexities in the upper part of the rupture not resolved by the inversion. However, any such conclusions would have to rely on more precise Green's functions, taking into account, e.g., all possible reverberations of the complex 3D valley in the area.

6.2. Effect of the Delayed Asperity

[41] As already explained above, the slip inversion in Paper 1 suggests approximately 3 s rupture delay of the southeastern deep asperity (Figure 4). Figure 9 shows comparison with observed data in terms of acceleration and velocity time series and normalized Husid plots (cumulative squared acceleration) for the best model and a model neglecting the asperity delay. Four stations, having different distances and positions around the fault and being sensitive to this particular source feature, are shown.

[42] The best-model seismograms (red traces in Figure 9) well reproduce the major features of the observed time series, such as acceleration envelope, velocity pulses and the high-frequency content of the records. Acceleration records exhibit two wave groups at stations AQA and GSA. They are well explained by the delayed asperity, as can be seen when compared with the synthetics for the non-delayed model (gray traces in Figure 9). Interestingly, at the other

two more distant stations (CLN and CSO) the two wave groups overlap. At these stations the non-delayed model results in early wave arrivals compared to what actually observed.

[43] In the velocity waveforms, the effect of the delayed asperity is best visible at CLN and partially at CSO and GSA stations. Indeed, at CLN, the model without the asperity delay exhibits a strong pulse at the beginning of the waveform, which is not present in the observed data. It is interesting to note that due to the position of CLN station with respect to the fault, the energy-time distribution is mainly controlled by the rupture time of the stronger SE asperity.

[44] The normalized Husid plots emphasize that the delayed-asperity results better capture the energy-time distribution of the observed data. Thus the broadband modeling confirms the significance of the rupture delay of the deeper asperity.

6.3. Effect of Rupture Velocity

[45] As explained in section 5, the best model is characterized by $V_r = 3$ km/s in the bottom part of the fault and $V_r = 2$ km/s in the upper part (see also Figure 4). Figure 10 shows the synthetic ground motions at AQA and GSA stations calculated for different rupture velocity values. As example, we show the acceleration and velocity seismograms obtained by removing the rupture velocity decrease in the shallow part of the fault and by extending the rupture velocity value in the shallow part to the whole fault. In the first

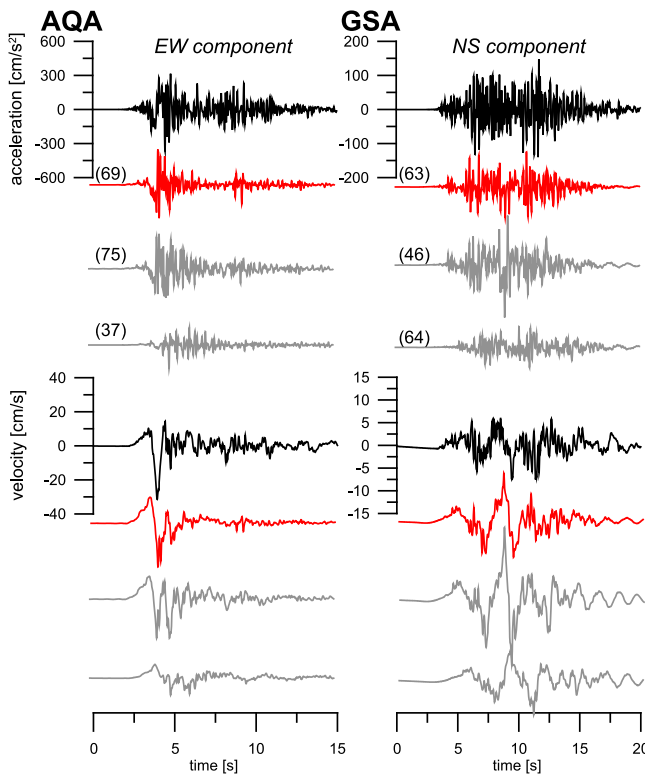


Figure 10. Effect of the rupture velocity. Recorded (black), best model (red), $V_r = 3$ km/s over the whole fault (gray, upper) and $V_r = 2$ km/s over the whole fault (gray, lower) ground-acceleration and velocity waveforms (one horizontal component) at two selected sites (indicated in Figure 1). The numbers between brackets are the goodness-of-fit score.

case (i.e., $V_r = 3$ km/s all over the fault) there is a clear enhancement of mid- and high-frequency amplitudes. The peak values are not substantially affected at AQA station and the major effect is the appearance of a second large velocity pulse whereas the first one remain unaffected. This second pulse is not observed in the recorded waveform suggesting that the first pulse is related to the initial phase of the updip rupture propagation (i.e., between the hypocenter and 5 km depth). At GSA stations the observed velocity amplitudes are largely overestimated, demonstrating that the rupture velocity decrease in the shallow part of the fault is necessary to correctly model this updip station.

[46] In the second example (i.e., $V_r = 2$ km/s all over the fault) the waveforms at AQA show much smaller amplitudes and no strong velocity pulse is observed. For GSA, the small rupture velocity does not have a large effect at velocity waveforms, while the acceleration record is rather underestimated.

6.4. Effect of Slip Distribution at High Wave Numbers

[47] As explained in Section 5 we constrained the positions of the three largest subsources at level $n = 2$ of the HIC source model in order to reproduce the distribution of asperities retrieved in Paper 1. At levels larger than 2 the remaining 60 subsources are randomly distributed over the fault plane following the defined number-size distribution, composing random high wave numbers details of the slip

distribution. The results presented so far are calculated using one single realization of the random distribution of these subsources (i.e., for one slip distribution). In Figure 11, we show the effect of 6 different realizations of the slip distributions, obtained by using different seeds in the random generator, on the ground acceleration and velocity simulated at AQA and GSA stations. As expected, the effect is stronger at AQA that is closer to the fault rupture, being sensitive to the details of the slip distribution. The ground motion amplitudes around 0.7–1 Hz are remarkably affected (mostly due to varying position of level 3 and 4 subsources) and, for some slip distributions, the velocity pulse amplitude decreases substantially. Examining the six models (labeled from 1 to 6 in Figure 11) we note that the larger low-frequency spectral content of models 1 and 5 with respect to the others is somehow related to the amount of slip “above” the hypocenter and toward the northwestern termination of the fault plane. At GSA station the six slip distributions produce less ground motion variations.

6.5. Effect of Crossover Frequency Band: From Integral to Composite Approach

[48] The crossover frequency range in the HIC model is a subject of choice. We remind the reader that this frequency divides the low-frequency (coherent/deterministic) and high-frequency (incoherent/stochastic) parts of the simulated wavefield. In other applications [Gallovič and Brokešová, 2007; Gallovič and Burjáněk, 2007; Ameri et al., 2009b; Zollo et al., 2009; Ameri et al., 2011], this range was set up around frequency of 1 Hz. The present application, dealing with stations located basically above the fault, deserves a more careful investigation of the crossover frequency value. Thus, Figure 12 shows comparison of observed velocities with synthetics for two crossover frequency ranges (1.5–2 Hz in red and 0.15–0.6 Hz in gray) at six selected stations around the fault located at increasing distance. The comparison is shown for velocity time series because (unlike the accelerations) the velocities are more sensitive to this low-to-intermediate frequency range. Note that when the crossover frequency range is set up to the smaller values, the HIC model becomes almost a purely composite model.

[49] At AQU and AQA stations, the arrival of the observed waveforms starts with a distinct onset and a strong directivity pulse. Both the onset and the pulse are better explained when the higher crossover frequency range is considered (i.e., 1.5–2 Hz). This means that the very close stations require the wavefield to arrive coherently up to the relatively high frequencies of 2 Hz. On the other hand, at GSA and CLN stations, located in the updip and along-strike rupture propagation directions, respectively, a better fit is obtained with the lower crossover frequency range (i.e., 0.15–0.6 Hz). At these stations, the integral part of the model produces too large low-frequency amplitudes due directivity effects that are not equally observed in the records. Slightly more distant stations, represented in Figure 12 by FMG and LSS (located in backward directivity directions) are less sensitive to this choice. Nevertheless, comparison of waveforms and FAS at these two and other stations indicate preference of lower crossover range.

[50] Figure 12 demonstrates that the use of higher crossover frequency range allows modeling the long-period pulses in velocity records observed at the closest stations by

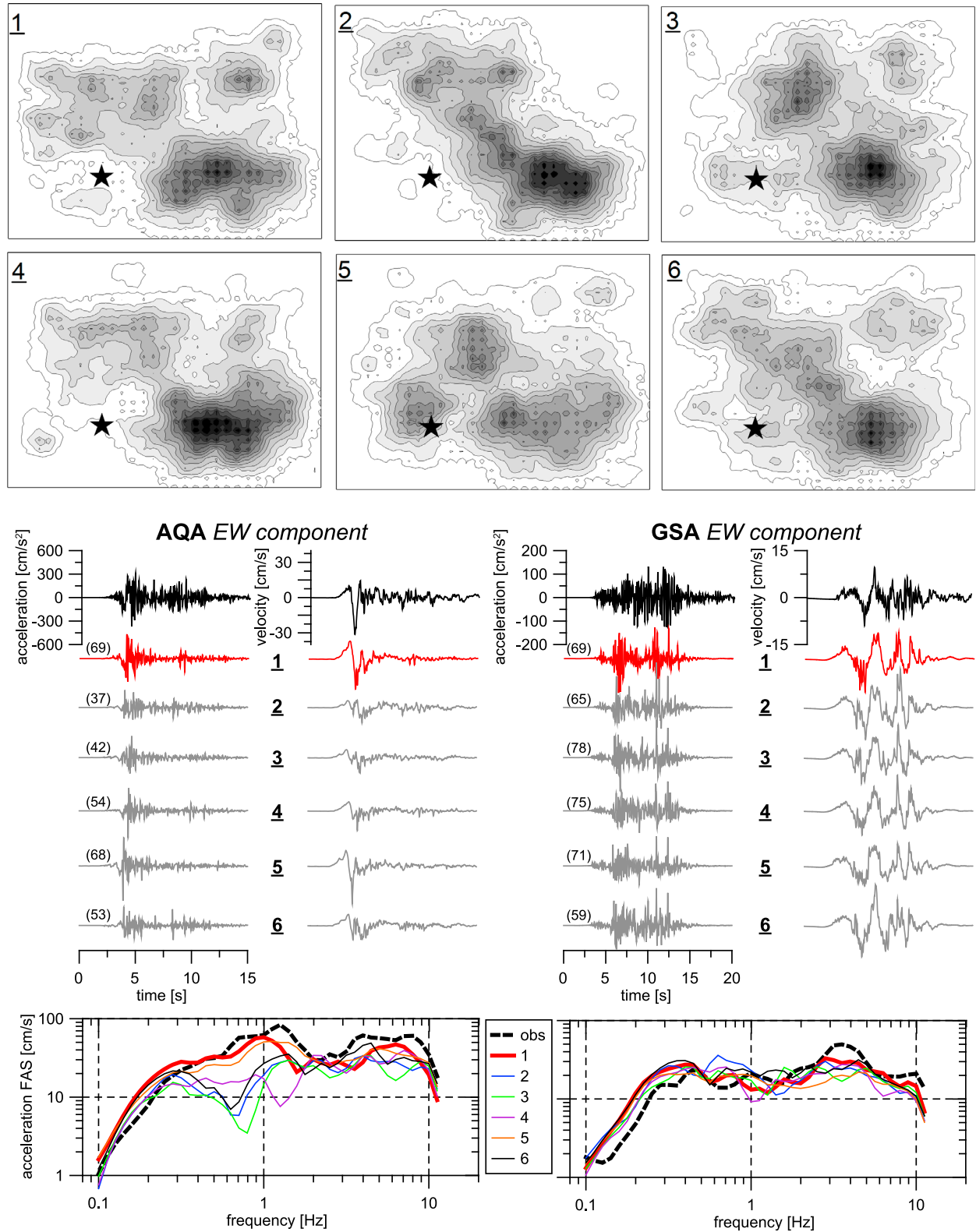


Figure 11. Effect of slip distribution at high wave numbers. (top) Six different slip models generated varying the random distribution of the small subsources (level > 2). The position of the largest subsources is kept constant. The black star represents the hypocenter. Model number 1 is the same reported in Figure 2. (middle) Recorded (black), best model (red) and different slip models (gray) ground-acceleration and velocity waveforms (one horizontal component) at two selected sites (indicated in Figure 1) are reported. The numbers between brackets are the goodness-of-fit score. (bottom) Corresponding smoothed acceleration Fourier amplitude spectra (FAS).

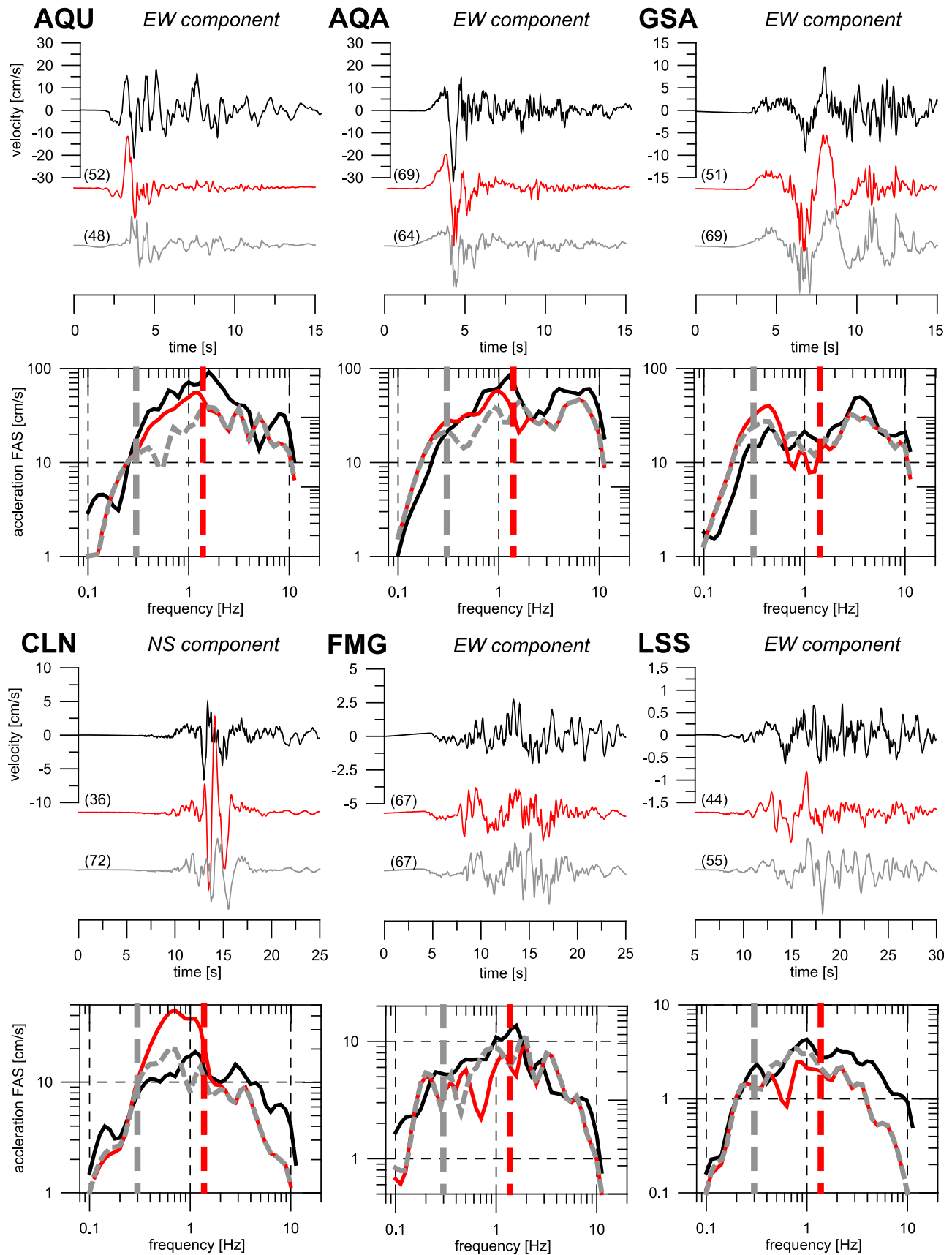


Figure 12

means of the integral approach. The lower frequency range for the further stations suggests that a purely deterministic modeling of rupture directivity is not suitable in this case, and that the stochastic (composite) approach is needed in almost the whole frequency band.

7. Discussion and Conclusions

[51] In the present paper we investigated the near-fault recordings of the Mw 6.3 2009 L'Aquila earthquake in a broad frequency range (up to 10 Hz) using a kinematic Hybrid Integral-Composite (HIC) earthquake source model. The recordings exhibited strong azimuthal and distance dependence. The main advantage of the HIC model was the consistent combination of low-frequency coherent and high-frequency incoherent ground motions, calculated by the use of the representation theorem and the composite approach, respectively. Several major parameters of the source model were constrained according to the preceding low-frequency (<0.2 Hz) inversion by means of the multiple finite-extent source model (see Paper 1). The considered stable major source parameters included position of the two main asperities (located, respectively, updip and southeast along-strike from the nucleation point), decrease of rupture velocity in the shallow part of the fault and time delay of the deeper asperity rupture. Other parameters of the HIC source model (namely, rupture velocity value, small scale slip distribution and stress drop) were investigated by comparison with observed records.

[52] The Green's functions were calculated in a 1D-layered crustal model including 1D soil profiles, where available, to account for site-specific response at the accelerometric stations. We demonstrated that the use of site-specific Green's functions improved the modeling results significantly in case of thick sediments layers (AVZ station). The variability observed at the considered near-fault sites was only partially related to local site amplification as it was also controlled by the rupture kinematics.

[53] Overall, the modeling results showed a remarkable fit with observed records despite the relative simplicity of the propagation models and the lack of site-specific amplification for most of the stations. Moreover, the decay of the observed PGA and PGV was better captured by synthetic values than by median estimates from regional GMPEs, suggesting that the predictions provided by such simple equations should be interpreted cautiously.

[54] We stress that in this study the broadband HIC source model, that was built on the basis of a low-frequency source inversion (see Paper 1), prescribes a coherent rupture for low-frequency seismograms and incoherent (complex) rupture for the high-frequency ones. Implicitly, the 'high-frequency' (HF) sources, representing the complex rupture, are located in the centers of the 'low-frequency' (LF) asperities. Note that such approach does not always guarantee successful modeling of broadband ground motions. For instance, for

huge (mostly) megathrust events there is an increasing evidence that the HF sources are adjacent to the LF asperities [Meng *et al.*, 2011a; Meng *et al.*, 2011b; Simons *et al.*, 2011; Koper *et al.*, 2011]. The small model bias across a wide frequency range supports the choice of the model parameters as well as the performance of the HIC approach to "extend" the low-frequency source model to higher frequencies, showing that, in the present case study, the HF radiation is co-located with the LF one. Nevertheless, a devoted study employing high-resolution back-projection techniques would have to be performed to eventually constrain the mutual location of the LF and HF sources.

[55] The main advantage of the modeling was that it allowed linking distinct features of the observed wavefield to particular source and propagation effects and provided insights on strong motion complexity from this moderate magnitude event. We showed that the source model complexities constrained from the kinematic inversion in the low-frequency range directly affected the strong-ground motion recordings also at higher frequencies. This was illustrated on example seismograms where the sensitivity to several source model features was shown.

[56] In particular, (1) the two slip asperities in the rupture model were necessary to explain the ground motion at the closest sites, where two distinct wave groups were clearly visible on recorded waveforms (e.g., AQ_, GSA stations). (2) The rupture delay of the southeastern asperity and the along-strike rupture propagation were essential to understand the CLN, GSA and CSO records. (3) The updip rupture propagation correctly explained the ground motion at GSA station. Tests regarding the effect of rupture velocity distribution on ground motion at this site showed that the decrease of rupture velocity in shallow part of fault was required to correctly fit the velocity waveforms, whereas larger rupture velocity values would have overestimated the observed amplitudes. (4) The near-fault AQ_ records were mainly controlled by the early phases of the rupture propagation that were responsible for the velocity pulses. The southeastern asperity, characterized by larger slip, generated the smaller later arrivals.

[57] The requirement of the rupture delay of the southeastern asperity to fit most of the near-fault records suggested that the earthquake might have experienced a first phase of rupture propagation in the updip direction and a second phase in the along-strike direction. It is not clear whether the two phases were separated by a rupture arrest or a slow-down of the rupture velocity. In any case, the earthquake can be regarded as a double event. Further studies should be performed to understand the dynamics of the L'Aquila earthquake in this respect.

[58] To obtain a better fit with the observed data we founded that the crossover frequency dividing the low-frequency coherent (integral) and high-frequency incoherent (composite) wavefields had to be variable, with larger values (>1.0 Hz) for the very close stations and smaller (<1 Hz)

Figure 12. Effect of the crossover frequency range. (top) Recorded (black) and simulated ground-velocity waveforms at six selected sites (indicated in Figure 1) are compared. The synthetics are calculated with two different crossover frequency ranges: 1.5–2 Hz (red waveforms) and 0.15–0.6 Hz (gray waveforms). The numbers between brackets are the goodness-of-fit score. (bottom) Smoothed acceleration Fourier amplitude spectra (FAS). Vertical lines mark the central frequencies of the lower (gray) and higher (red) frequency bands. Note that in this figure (unlike the others) the red seismograms does not represent the best model in all cases.

for more distant stations. Note that, typically, broadband simulation methods that combine the deterministic calculations at low frequency with stochastic approaches at high frequencies, use central crossover frequency constant at 1 Hz [e.g., Kamae *et al.*, 1998; Hartzell *et al.*, 1999; Graves and Pitarka, 2010]. This choice is based on the seismological observation that source radiation and wave-propagation effects tend to become random at frequencies above $f \approx 1$ Hz [e.g., Pulido and Kubo, 2004]. However, it sounds reasonable to expect that the frequency of transition between coherent and incoherent contributions varies also with magnitude and with distance [Frankel, 2009; Mai *et al.*, 2010]. Frankel [2009] investigated the magnitude dependence of the transition frequency by comparing simulated spectral accelerations from scenario events with empirical GMPEs. He used a transition frequency of 2.4 Hz for the Mw 6.5 ground motion simulations, which is close to our crossover frequency-band upper limit for the AQ₊ stations. However, it is hard to compare his and our results because: (1) Frankel assumed the transition frequency based on comparison of strike-normal and strike-parallel Fourier spectra recorded at Rinaldi near-fault station during the Mw 6.7 Northridge earthquake; and (2) the distance dependence of the transition frequency was not investigated by the author. Spudich and Chiou [2006] compared the strike-normal to strike-parallel ratio of spectral acceleration for NGA strong motion data set (for Mw > 6) with that calculated from an approximation of theoretical double-couple S-wave radiation pattern in order to find an optimal water level preventing zero amplitudes in nodal directions. Indeed their results can be seen as an indication of the coherent/incoherent character of the records as a function of source-to-site distance and frequency. Spudich and Chiou [2006] indicated that the effect of theoretical radiation pattern, that we modeled in the integral part of the method, was seen in the data at very close distances (0–5 km from the rupture) even at relatively high frequencies (~ 2 Hz) whereas it decreased with increasing distances with a trend depending on the frequency.

[59] Our finding of the different preference of the crossover frequency (i.e., 1.5 Hz and 0.3 Hz central frequencies, Figure 5) by close and distant stations on one hand supports the distance dependence of the crossover frequency, ascribing propagation effects as the main cause of incoherency of ground motions. On the other hand, the updip propagation along the first asperity could have been very smooth (i.e., associated with negligible variations of the rupture parameters), without generating much incoherent high-frequency radiation. In this hypothesis we assume that the incoherency of the observed wavefield is mainly linked to heterogeneity of the source process. Combination of both features is most likely. This topic should be further investigated using near- and far-fault strong motion data from other earthquakes and dynamic modeling of heterogeneous ruptures.

[60] Concerning the near-fault AQ₊ stations we have to admit that, although the main features of the waveforms were well reproduced, particularly for the east-west and vertical component, the simulations still pose some problems and we lacked energy after the large-amplitude arrivals. Critical aspects in this regard are: (1) the proximity of the stations to the point-sources, that may cause problem in the composite part (high-frequency) of the model; (2) the more complex radiation pattern for near-fault stations with respect

to the simple double-couple radiation pattern adopted in HIC model at low-frequencies [Pulido and Kubo, 2004]. We tested that small variations of the fault strike in the low-frequency calculations did not eliminate the underestimation of the N-S component. This limitation likely lies in the use of a 1D crustal model whereas a fault embedded in a 3D medium would perhaps improve the modeling of radiation pattern even at low frequencies [e.g., Gallovič *et al.*, 2010]. (3) The slip distribution (at small scale) in the vicinity of the hypocenter. The variability of the ground motion for different high wave numbers slip distributions was noticeable in some case and we cannot exclude that some model could enhance the North-South amplitudes. Indeed, we stress that the high wave numbers details of the slip distribution that we used in this paper as “best model” should not be acknowledged as the best slip model for the earthquake. As such, it is only the best among the few tested random distributions in explaining the records, i.e., capturing the main broadband features of the near-fault records. However, some other high wave numbers random slip distribution could provide similar or better fit to the data, although determining such model cannot be the aim of this paper due to the other limitations of the modeling. (4) 3D site-effects due to wave propagation within the Aterno Valley basin might be important to explain the ground motions observed at AQ₊ stations. Further studies should be performed in order to investigate the different causes.

[61] The presented results have strong conclusions not only to earthquake physics (see also Paper 1), but also to ground-motion simulations for hazard analyses and earthquake engineering applications. The set of scenario events should be enriched to include also models with characteristics found for the L'Aquila earthquake. The doublet character of the event has direct consequences on duration of the records, that is critical to assess the cyclic seismic response of structures. The variable crossover frequency, playing an important role especially at near-fault distances, should be also taken into account in scenario studies. Purely composite and/or stochastic models without the possibility of modeling the coherent low-frequency wavefield by the integral approach would meet difficulties when explaining the near-source directivity pulses observed at AQ₊ stations. Correct modeling of pulse-type records is of great relevance to earthquake engineering because their seismic demand and spectral shape are different with respect to ordinary records and can generate much higher damage.

[62] **Acknowledgments.** The authors acknowledge free Internet access of waveforms provided by the Italian Strong Motion Database (ITACA, <http://itaca.mi.ingv.it/>). Financial support from Project RS1 (ReLUIS-DPC 2010–2013), NERA 262330, GACR 210/11/0854, MSM0021620860. We thank Kim Olsen for providing the GOF code and Rodolfo Puglia for providing the soil profiles used in the calculations. We particularly thank Jiří Zahradník for fruitful discussions. Finally, we acknowledge the constructive comments of the Associate Editor Martin Mai and of two anonymous reviewers that significantly improved the paper.

References

- Aagaard, B. T., *et al.* (2008), Ground-motion modeling of the 1906 San Francisco earthquake, part II: Ground-motion estimates for the 1906 earthquake and scenario events, *Bull. Seismol. Soc. Am.*, 98, 1012–1046, doi:10.1785/0120060410.
- Akinci, A., L. Malagnini, and F. Sabetta (2010), Characteristics of the strong ground motions from the 6 April 2009 L'Aquila earthquake,

- Italy, *Soil. Dyn. Earthquake Eng.*, 30, 320–335, doi:10.1016/j.soildyn.2009.12.006.
- Ameri, G., F. Pacor, G. Cultrera, and G. Franceschina (2008), Deterministic ground-motion scenarios for engineering applications: The case of Thessaloniki, Greece, *Bull. Seismol. Soc. Am.*, 98(3), 1289–1303, doi:10.1785/0120070114.
- Ameri, G., et al. (2009a), The 6 April 2009, M_w 6.3, L'Aquila (central Italy) earthquake: Strong-motion observations, *Seismol. Res. Lett.*, 80, 951–966, doi:10.1785/gssrl.80.6.951.
- Ameri, G., F. Gallovič, F. Pacor, and A. Emolo (2009b), Uncertainties in strong ground-motion prediction with finite-fault synthetic seismograms: An application to the 1984 M 5.7 Gubbio, central Italy, earthquake, *Bull. Seismol. Soc. Am.*, 99, 647–663, doi:10.1785/0120080240.
- Ameri, G., A. Emolo, F. Pacor, and F. Gallovič (2011), Ground-motion simulations for the M 6.9 Irpinia 1980 earthquake (southern Italy) and scenario events, *Bull. Seismol. Soc. Am.*, 101(3), 1136–1151, doi:10.1785/0120100231.
- Anderson, J. G., and S. E. Hough (1984), A model for the shape of the Fourier amplitude spectrum of acceleration at high frequencies, *Bull. Seismol. Soc. Am.*, 74, 1969–1993.
- Andrews, D. J. (1980), A stochastic fault model: 1. Static case, *J. Geophys. Res.*, 85, 3867–3877, doi:10.1029/JB085iB07p03867.
- Anzidei, M., et al. (2009), Coseismic deformation of the destructive April 6, 2009 L'Aquila earthquake (central Italy) from GPS data, *Geophys. Res. Lett.*, 36, L17307, doi:10.1029/2009GL039145.
- Atzori, S., I. Hunstad, M. Chini, S. Salvi, C. Tolomei, C. Bignami, S. Stramondo, E. Trasatti, A. Antonioli, and E. Boschi (2009), Finite fault inversion of DInSAR coseismic displacement of the 2009 L'Aquila earthquake (central Italy), *Geophys. Res. Lett.*, 36, L15305, doi:10.1029/2009GL039293.
- Bianchi, I., C. Chiarabba, and N. Piana Agostinetti (2010), Control of the 2009 L'Aquila earthquake, central Italy, by a high-velocity structure: A receiver function study, *J. Geophys. Res.*, 115, B12326, doi:10.1029/2009JB007087.
- Bindi, D., R. R. Castro, G. Franceschina, L. Luzi, and F. Pacor (2004), The 1997–1998 Umbria-Marche sequence (central Italy): Source, path, and site effects estimated from strong motion data recorded in the epicentral area, *J. Geophys. Res.*, 109, B04312, doi:10.1029/2003JB002857.
- Bindi, D., F. Pacor, L. Luzi, M. Massa, and G. Ameri (2009), The M_w 6.3, 2009 L'Aquila earthquake: Source, path and site effects from spectral analysis of strong motion data, *Geophys. J. Int.*, 179, 1573–1579, doi:10.1111/j.1365-246X.2009.04392.x.
- Bindi, D., F. Pacor, L. Luzi, R. Puglia, M. Massa, G. Ameri, and R. Paolucci (2011), Ground motion prediction equations derived from the Italian strong motion data base, *Bull. Earthquake Eng.*, 9(6), 1899–1920, doi:10.1007/s10518-011-9313-z.
- Boatwright, J. (2007), The persistence of directivity in small earthquakes, *Bull. Seismol. Soc. Am.*, 97, 1850–1861, doi:10.1785/0120050228.
- Bouchon, M. (1981), A simple method to calculate Green's functions for elastic layered media, *Bull. Seismol. Soc. Am.*, 71, 959–971.
- Comité Européen de Normalisation (2004), Eurocode 8: Design of structures for earthquake resistance—Part 1: General rules, seismic actions and rules for buildings, *Rep. EN 1998-1:2004*, Brussels.
- Chiarabba, C., et al. (2009), The 2009 L'Aquila (central Italy) M_w 6.3 earthquake: Main shock and aftershocks, *Geophys. Res. Lett.*, 36, L18308, doi:10.1029/2009GL039627.
- Chioccarelli, E., and I. Iervolino (2010), Near-source seismic demand and pulse-like records: A discussion for L'Aquila earthquake, *Earthquake Eng. Struct. Dyn.*, 39, 1039–1062.
- Cirella, A., A. Piatanesi, M. Cocco, E. Tinti, L. Scognamiglio, A. Michelini, A. Lomax, and E. Boschi (2009), Rupture history of the 2009 L'Aquila (Italy) earthquake from non-linear joint inversion of strong motion and GPS data, *Geophys. Res. Lett.*, 36, L19304, doi:10.1029/2009GL039795.
- Cultrera, G., F. Pacor, G. Franceschina, A. Emolo, and M. Cocco (2009), Directivity effects for moderate-magnitude earthquakes (M_w 5.6–6.0) during the 1997 Umbria–Marche sequence, central Italy, *Tectonophysics*, 476, 110–120, doi:10.1016/j.tecto.2008.09.022.
- Cultrera, G., M. Mucciarelli, and S. Parolai (2011), The L'Aquila earthquake—A view of site effects and building behavior from temporary networks, *Bull. Earthquake Eng.*, 9(3), 691–695, doi:10.1007/s10518-011-9270-6.
- D'Amico, S., K. D. Koper, R. B. Herrmann, A. Akinci, and L. Malagnin (2010), Imaging the rupture of the M_w 6.3 April 6, 2009 L'Aquila, Italy, earthquake using back-projection of teleseismic P-waves, *Geophys. Res. Lett.*, 37, L03301, doi:10.1029/2009GL042156.
- Di Capua, G. (2009), Progress report on the ongoing activity for constructing a catalogue of geological/geotechnical information at accelerometer stations, *Rep. INGV-DPC 2007-2009*, Ist. Naz. di Geofis. e Vulcanol., Rome. [Available at http://esse4.mi.ingv.it/images/stories/deliverable_d4.pdf]
- Di Capua, G., G. Lanzo, V. Pessina, S. Peppoloni, and G. Scasserra (2011), The recording stations of the Italian strong motion network: Geological information and site classification, *Bull. Earthquake Eng.*, 9(6), 1779–1796, doi:10.1007/s10518-011-9326-7.
- Faluccci, E., et al. (2009), The Paganica fault and surface coseismic ruptures caused by the 6 April 2009 earthquake (L'Aquila, central Italy), *Seismol. Res. Lett.*, 80(6), 940–950, doi:10.1785/gssrl.80.6.940.
- Frankel, A. (2009), A constant stress-drop model for producing broadband synthetic seismograms: Comparison with the next generation attenuation relations, *Bull. Seismol. Soc. Am.*, 99, 664–680, doi:10.1785/0120080079.
- Gallovič, F., and J. Brokešová (2004), On strong ground motion synthesis with k^{-2} slip distributions, *J. Seismol.*, 8, 211–224, doi:10.1023/B:JOSE.0000021438.79877.58.
- Gallovič, F., and J. Brokešová (2007), Hybrid k -squared source model for strong ground motion simulations: Introduction, *Phys. Earth Planet. Inter.*, 160, 34–50, doi:10.1016/j.pepi.2006.09.002.
- Gallovič, F., and J. Burjánek (2007), High-frequency directivity in strong ground motion modeling methods, *Ann. Geophys.*, 50(2), 203–211.
- Gallovič, F., and J. Zahradník (2011), Complexity of the $M_{6.3}$ 2009 L'Aquila (central Italy) earthquake: 1. Multiple finite-extent source inversion, *J. Geophys. Res.*, 117, B04307, doi:10.1029/2011JB008709.
- Gallovič, F., M. Kaser, J. Burjánek, and C. Papaioannou (2010), Three-dimensional modeling of near-fault ground motions with nonplanar rupture models and topography: Case of the 2004 Parkfield earthquake, *J. Geophys. Res.*, 115, B03308, doi:10.1029/2008JB006171.
- Graves, R. W., and A. Pitarka (2010), Broadband ground-motion simulation using a hybrid approach, *Bull. Seismol. Soc. Am.*, 100, 2095–2123, doi:10.1785/0120100057.
- Graves, R. W., B. T. Aagaard, and K. W. Hudnut (2011), The ShakeOut earthquake source and ground motion simulations, *Earthquake Spectra*, 27, 273–291, doi:10.1193/1.3570677.
- Gruppo di Lavoro, M. S.-A. Q. (2010), Microzonazione sismica per la ricostruzione dell'area aquilana (in Italian), report, 769 pp., Dip. della Protezione Civ., Regione Abruzzo, Italy. [Available at http://www.protezionecivile.gov.it/jcms/it/view_pub.wp?contentId=PUB25330.]
- Hartzell, S., S. Harmsen, A. Frankel, and S. Larsen (1999), Calculation of broadband time histories of ground motion: Comparison of methods and validation using strong-ground motion from the 1994 Northridge earthquake, *Bull. Seismol. Soc. Am.*, 89, 1484–1504.
- Herrero, A., and P. Bernard (1994), A kinematic self-similar rupture process for earthquakes, *Bull. Seismol. Soc. Am.*, 84, 1216–1228.
- Hisada, Y. (2008), Broadband strong motion simulation in layered half-space using stochastic Green's function technique, *J. Seismol.*, 12, 265–279, doi:10.1007/s10950-008-9090-6.
- Kamae, K., K. Irikura, and A. Pitarka (1998), A technique for simulating strong ground motions using hybrid Green's functions, *Bull. Seismol. Soc. Am.*, 88, 357–367.
- Koper, K. D., A. R. Hutko, T. Lay, C. J. Ammon, and H. Kanamori (2011), Frequency-dependent rupture process of the 11 March 2011 M_w 9.0 Tohoku earthquake: Comparison of short-period P wave back-projection images and broadband seismic rupture models, *Earth Planets Space*, 58, 1–4.
- Lanzo, G., M. Tallini, G. Milana, G. Di Capua, F. Del Monaco, A. Pagliaroli, and S. Peppoloni (2011), The Aterno Valley strong-motion array: Seismic characterization and determination of subsoil model, *Bull. Earthquake Eng.*, 9, 1855–1875.
- Mai, P. M., and G. C. Beroza (2003), A hybrid method for calculating near-source, broadband seismograms: Application to strong motion prediction, *Phys. Earth Planet. Inter.*, 137, 183–199, doi:10.1016/S0031-9201(03)00014-1.
- Mai, P. M., W. Imperatori, and K. B. Olsen (2010), Hybrid broadband ground-motion simulations: Combining long-period deterministic synthetics with high-frequency multiple S-to-S backscattering, *Bull. Seismol. Soc. Am.*, 100(5A), 2124–2142, doi:10.1785/0120080194.
- Meng, L., A. Inbal, and J.-P. Ampuero (2011a), A window into the complexity of the dynamic rupture of the 2011 M_w 9 Tohoku-Oki earthquake, *Geophys. Res. Lett.*, 38, L00G07, doi:10.1029/2011GL048118.
- Meng, L., J.-P. Ampuero, A. Sladen, and H. Rendell (2011b), High-resolution back-projection at regional distance: Application to the Haiti $M_{7.0}$ earthquake and comparisons with finite source studies, *J. Geophys. Res.*, doi:10.1029/2011JB008702, in press.
- Olsen, K. B., and J. E. Mayhew (2010), Goodness-of-fit criteria for broadband synthetic seismograms, with application to the 2008 $M_{5.4}$ Chino Hills, CA, earthquake, *Seismol. Res. Lett.*, 81, 715–723, doi:10.1785/gssrl.81.5.715.
- Pitarka, A., P. Somerville, Y. Fukushima, T. Uetake, and K. Irikura (2000), Simulation of near-fault strong-ground motion using hybrid Green's function, *Bull. Seismol. Soc. Am.*, 90(3), 566–586, doi:10.1785/0119990108.

- Puglia, R., R. Dittommaso, F. Pacor, M. Mucciarelli, L. Luzi, and M. Bianca (2011), Frequency variation in site response as observed from strong motion data of the L'Aquila (2009) seismic sequence, *Bull. Earthquake Eng.*, 9(3), 869–892, doi:10.1007/s10518-011-9266-2.
- Pulido, N., and T. Kubo (2004), Near-fault strong-motion complexity of the 2000 Tottori earthquake (Japan) from a broadband asperity model, *Tectonophysics*, 390, 177–192, doi:10.1016/j.tecto.2004.03.032.
- Scognamiglio, L., E. Tinti, A. Michelini, D. S. Dreger, A. Cirella, M. Cocco, S. Mazza, and A. Piatanesi (2010), Fast determination of moment tensors and rupture history: What has been learned from the 6 April 2009 L'Aquila earthquake sequence, *Seismol. Res. Lett.*, 81, 892–906, doi:10.1785/gssrl.81.6.892.
- Simons, M., et al. (2011), The 2011 magnitude 9.0 Tohoku-Oki earthquake: Mosaicking the megathrust from seconds to centuries, *Science*, 332, 1421–1425, doi:10.1126/science.1206731.
- Somerville, P. G., N. F. Smith, R. W. Graves, and N. A. Abrahamson (1997), Modification of empirical strong ground motion attenuation relations to include the amplitude and duration effects of rupture directivity, *Seismol. Res. Lett.*, 68, 199–222, doi:10.1785/gssrl.68.1.199.
- Spudich, P., and B. S.-J. Chiou (2006), Directivity in preliminary NGA residuals, Final Project Report for PEER Lifelines Program Task 1M01, *Rep. SASI46-15811*, 49 pp., Pac. Earthquake Eng. Res. Cent., Berkeley, Calif.
- Spudich, P., and B. S. Chiou (2008), Directivity in NGA earthquake ground motions: Analysis using isochrone theory, *Earthquake Spectra*, 24(1), 279–298, doi:10.1193/1.2928225.
- Zambonelli, E., R. de Nardis, L. Filippi, M. Nicoletti, and M. Dolce (2011), Performance of the Italian strong motion network during the 2009, L'Aquila seismic sequence (central Italy), *Bull. Earthquake Eng.*, 9, 39–65, doi:10.1007/s10518-010-9218-2.
- Zeng, Y., J. G. Anderson, and G. Yu (1994), A composite source model for computing realistic synthetic strong ground motions, *Geophys. Res. Lett.*, 21, 725–728, doi:10.1029/94GL00367.
- Zollo, A., et al. (2009), The earthquake early warning system in southern Italy: Methodologies and performance evaluation, *Geophys. Res. Lett.*, 36, L00B07, doi:10.1029/2008GL036689.

G. Ameri and F. Pacor, Istituto Nazionale di Geofisica e Vulcanologia, via Bassini 15, I-20133 Milan, Italy. (gabriele.ameri@mi.ingv.it)

F. Gallovič, Faculty of Mathematics and Physics, Department of Geophysics, Charles University, V Holesovickach 2, Praha 8, Prague 180 00, Czech Republic.